

**LINEAR-REGRESSION CONVOLUTIONAL NEURAL
NETWORK FOR FULLY AUTOMATED CORONARY LUMEN
SEGMENTATION IN INTRAVASCULAR OPTICAL
COHERENCE TOMOGRAPHY**

YONG YAN LING

**FACULTY OF ENGINEERING
UNIVERSITY OF MALAYA
KUALA LUMPUR**

2018

**LINEAR-REGRESSION CONVOLUTIONAL NEURAL
NETWORK FOR FULLY AUTOMATED CORONARY LUMEN
SEGMENTATION IN INTRAVASCULAR OPTICAL
COHERENCE TOMOGRAPHY**

YONG YAN LING

**DISSERTATION SUBMITTED IN FULFILMENT OF
THE REQUIREMENTS FOR THE DEGREE OF MASTER
OF ENGINEERING SCIENCE**

**DEPARTMENT OF BIOMEDICAL ENGINEERING
FACULTY OF ENGINEERING
UNIVERSITY OF MALAYA
KUALA LUMPUR**

2018

UNIVERSITY OF MALAYA
ORIGINAL LITERARY WORK DECLARATION

Name of Candidate: Yong Yan Ling

Matric No: KGA150024

Name of Degree: Master of Engineering Science

Title of Project Paper/Research Report/Dissertation/Thesis (“this Work”):

Linear-Regression Convolutional Neural Network For Fully Automated Coronary Lumen Segmentation In Intravascular Optical Coherence Tomography

Field of Study: Biomedical Engineering

I do solemnly and sincerely declare that:

- (1) I am the sole author/writer of this Work;
- (2) This Work is original;
- (3) Any use of any work in which copyright exists was done by way of fair dealing and for permitted purposes and any excerpt or extract from, or reference to or reproduction of any copyright work has been disclosed expressly and sufficiently and the title of the Work and its authorship have been acknowledged in this Work;
- (4) I do not have any actual knowledge nor do I ought reasonably to know that the making of this work constitutes an infringement of any copyright work;
- (5) I hereby assign all and every rights in the copyright to this Work to the University of Malaya (“UM”), who henceforth shall be owner of the copyright in this Work and that any reproduction or use in any form or by any means whatsoever is prohibited without the written consent of UM having been first had and obtained;
- (6) I am fully aware that if in the course of making this Work I have infringed any copyright whether intentionally or otherwise, I may be subject to legal action or any other action as may be determined by UM.

Candidate’s Signature

Date:

Subscribed and solemnly declared before,

Witness’s Signature

Date:

Name:

Designation:

**LINEAR-REGRESSION CONVOLUTIONAL NEURAL NETWORK FOR
FULLY AUTOMATED CORONARY LUMEN SEGMENTATION IN
INTRAVASCULAR OPTICAL COHERENCE TOMOGRAPHY**

ABSTRACT

Intravascular optical coherence tomography (IVOCT) is an optical imaging modality commonly used in the assessment of coronary artery diseases during percutaneous coronary intervention (PCI). Manual segmentation to assess luminal stenosis from OCT pullback scans is time consuming as each pullback contains hundreds of cross-sectional images. This segmentation is also challenging and susceptible to inter-observer variability due to various reasons including non-homogenous image intensity, blood residue, the presence and absence of different types of stents, irregular lumen shapes, image artifacts, and bifurcations. In this study, we aim to facilitate the quantitative assessment of coronary artery stenosis during PCI by developing an automatic segmentation framework to extract lumen from IVOCT images using convolutional neural network (CNN). A combination of linear-regression and convolutional neural network was proposed to automatically perform vessel lumen segmentation, parameterized in terms of radial distances from the catheter centroid in polar space. This automated segmentation algorithm has been benchmarked against manual segmentation by human experts. The proposed algorithm achieved an average locational accuracy of the vessel wall of 22 microns; 0.985 and 0.970 in Dice coefficient and Jaccard similarity index, respectively when compared against the gold standard manual segmentations. The average absolute error of luminal area estimation is 1.38 % and the processing rate is 40.6 ms per image. In addition, an inter-observer variability test was performed and has shown that the proposed algorithm has comparable variability against manual luminal area estimations by expert human observers. As a conclusion, the proposed image segmentation framework has the potential to be

incorporated into a clinical workflow and to facilitate quantitative assessment of vessel lumen in an intra-operative timeframe.

Keywords: convolutional neural network, optical coherence tomography, coronary artery disease, image segmentation, coronary lumen

University of Malaya

**REGRESI LINEAR RANGKAIAN NEURAL KONVOLUSI UNTUK
SEGMENTASI AUTOMATIK LUMEN KORONARI DALAM TOMOGRAFI
KOHEREN OPTIK INTRAVASKULAR**

ABSTRAK

Tomografi koheren optik intravaskular (IVOCT) merupakan modaliti pengimejan yang biasa digunakan dalam penilaian penyakit koronari arteri semasa intervensi koronari perkutaneus (PCI). Segmentasi manual untuk menilai stenosis luminal daripada imbasan tarik balik OCT merupakan satu proses yang mengambil masa yang lama kerana setiap tarik balik mengandungi ratusan imej keratan rentas. Segmentasi sebegini adalah sukar dan terdedah kepada kebolehubahan antara pemerhati. Perkara ini adalah disebabkan oleh intensiti imej yang tidak seragam, residu darah, kepelbagaian stent, ketidakseragaman bentuk lumen, artifak imej, dan percabangan arteri. Objektif kajian ini adalah untuk mempermudah penilaian kuantitatif stenosis koronari arteri semasa PCI dengan membangunkan rangka kerja segmentasi automatik untuk mengekstrak lumen daripada imej IVOCT dengan menggunakan rangkaian neural konvolusi (CNN). Cadangan kami adalah untuk menggabungkan regresi linear dan rangkaian neural konvolusi untuk mensegmen lumen melalui jarak radial daripada centroid kateter di dalam ruang polar. Segmentasi automatik ini telah ditanda aras dengan segmentasi manual oleh pakar. Algoritma segmentasi kami mencapai purata ketepatan lokasi dinding lumen sebanyak 22 mikron; 0.985 dan 0.970 dalam koefisien Dice dan index persamaan Jaccard masing-masing apabila dibandingkan dengan segmentasi manual piawai emas. Purata ralat mutlak anggaran keluasan luminal adalah 1.38% dan kadar pemrosesan adalah 40.6 ms setiap imej. Tambahan pula, kajian kebolehubahan antara pemerhati juga dijalankan dan hasilnya menunjukkan bahawa algoritma yang dicadangkan adalah hampir serupa dengan anggaran keluasan luminal oleh pakar. Kesimpulan kami adalah cadangan rangka kerja segmentasi kami berpotensi untuk

diperbadankan dalam aliran kerja klinikal dan mampu mempermudah penilaian kuantitatif saluran lumen dalam jangka masa intra-operasi.

Kata kunci: rangkaian neural konvolusi, tomografi koheren optic, penyakit koronari arteri, segmentasi imej, saluran koronari.

University of Malaya

ACKNOWLEDGEMENTS

It is with great pleasure for me to express my gratitude and acknowledgement to the parties which have been involved in this research. First and foremost, I would like to thank Ir. Dr. Liew Yih Miin and Prof. Dr. Chee Kok Han for their supervision during the course of the study.

In addition, I would also extend my gratitude to Prof. Robert A. McLaughlin from the University of Adelaide and Mr. Tan Li Kuo from University of Malaya for their guidance, insights and input during the period this research was conducted.

I would also like to extend my gratitude to the staff and clinicians of the University Malaya Medical Centre for their assistance during the process of medical image acquisition.

Lastly, I would also like to thank the undergraduate and post-graduate students who assisted in the study.

TABLE OF CONTENTS

Abstract	iii
Abstrak	v
Acknowledgements	vii
Table of Contents	viii
List of Figures	x
List of Tables.....	xii
List of Symbols and Abbreviations.....	xiii
CHAPTER 1: INTRODUCTION.....	1
1.1 Problem statements.....	1
1.2 Objectives	2
1.3 Thesis Outline.....	2
CHAPTER 2: LITERATURE REVIEW.....	4
2.1 Cardiovascular disease and Coronary Artery Disease.....	4
2.2 Imaging modalities of coronary artery disease assessment	5
2.2.1 X-ray angiography.....	5
2.2.2 Computed tomography (CTA)	6
2.2.3 Cardiac Magnetic Resonance Imaging (CMR)	7
2.2.4 Intravascular Ultrasound (IVUS)	7
2.3 Optical coherence tomography	9
2.3.1 Segmentation of optical coherence tomography	13
2.4 Neural networks.....	19
2.4.1 Background and intuition of neural networks	21
2.5 Optical coherence tomography and convolutional neural networks.....	23

2.6	Summary.....	24
CHAPTER 3: METHODOLOGY.....		25
3.1	IVOCT data acquisition and preparation for training and testing	25
3.2	CNN regression architecture & implementation details.....	26
3.3	Validation	28
3.4	Dependency of network performance on training data quantity	29
3.5	Inter-observer variability against CNN accuracy	30
CHAPTER 4: RESULTS.....		31
4.1	Dependency of network performance on training data quantity	31
4.2	Inter-observer variability against CNN accuracy	36
CHAPTER 5: DISCUSSION		37
CHAPTER 6: CONCLUSION.....		40
6.1	Future works	40
	References	41
	List of Publications and Papers Presented	46
	APPENDIX A	47

LIST OF FIGURES

Figure 2.1: An image of a X-ray angiogram (Auricchio, Conti, Ferrazzano, & Sgueglia, 2014).	6
Figure 2.2: (a) Normal coronary artery visualized using IVUS. (b) A segment of showing layers of the coronary artery wall. The intima is the white stripe indicated by the black arrows. The media is indicated by the black sonolucent band beyond the intima. The adventitia is indicated by the bright white area beyond the media (De Franco & Nissen, 2001).	8
Figure 2.3: Normal artery wall comprising of the intima, media and adventitia visualized using intravascular OCT (Guillermo J. Tearney et al., 2012).....	10
Figure 2.4: Scheme of TD-OCT (top) and FD-OCT (bottom). From (Bezerra et al., 2009)	11
Figure 2.5: A B-scan (left) and an axial scan of an OCT image (right). From (Wang et al., 2013).	12
Figure 2.6: Image processing framework proposed by (Celi & Berti, 2014).	16
Figure 2.7: General structure of a neural network with two hidden layers. w_{ij} indicates the weights of the link between layers (Amato et al., 2013).....	20
Figure 3.1: Overview of the linear-regression CNN segmentation system (refer to text for details).	27
Figure 4.1: Mean absolute error against different numbers of training data sets.....	31
Figure 4.2: Representative results from the test sets, showing good segmentation from linear-regression CNN on images with good lumen border contrast (a), inhomogenous lumen intensity (b), severe stenosis (c), blood swirl due to inadequate flushing (d)-(f), multiple reflections (indicated by yellow arrow) (g), embedded metallic and bioresorbable stent struts due to restenosis in (h) & (i) respectively, malapposed metallic stent struts (j), malapposed bioresorbable stent strut (k), and minor side branch (l). Blue and red contours represent CNN segmentation and gold standard, respectively. Scale bar (a) represents 500 microns.	33
Figure 4.3: Representative cases from the test sets, showing reasonable lumen segmentation from linear-regression CNN on images with medium-sized bifurcations (a-b). Poorer results were seen at major bifurcations (c-d), where the appropriate boundary for segmenting the main vessel was ambiguous. Blue and red contours represent CNN segmentation and gold standard, respectively. Scale bar (a) represents 500 microns.	34

Figure 4.4: Reconstruction of vessel wall from two different pullbacks for visual comparison of CNN regression segmentation against the gold standard manual segmentation. Vessel walls (left and middle columns) are color-coded with cross-sectional luminal area. Difference in luminal area is displayed on the right. All the axis is in mm and colorbar indicates luminal area in mm². 35

Figure 4.5: Bland-Altman plot analysis of luminal area for all possible pair-comparisons between different observers (a) and between CNN and observers (b) for the 100 randomly selected images from the test set. 36

University of Malaya

LIST OF TABLES

Table 3.1: Linear-regression CNN architecture for lumen segmentation at each windowed image. The output is the radial distance at the lumen border from the center of the catheter. CN: convolutional layer, FC: fully-connected layer.	28
Table 4.1: Accuracy of CNN segmentation with 45 training pullbacks (n = 13,342). The values are obtained based on the segmentation on 19 test pullbacks (n = 5,685).....	32
Table 4.2: Luminal area in 19 test pullbacks with optimal training	34

University of Malaya

LIST OF SYMBOLS AND ABBREVIATIONS

ANN	:	Artificial neural network
CTA	:	Computed tomography coronary angiography
CNN	:	Convolutional neural network
CAD	:	Coronary artery disease
IVOCT	:	Intravascular Optical Coherence Tomography
IVUS	:	Intravascular ultrasound
PCI	:	Percutaneous Coronary Intervention

University of Malaya

CHAPTER 1: INTRODUCTION

Cardiovascular disease is the leading cause of death globally (World Health Organization, 2014). Atherosclerosis of the coronary artery disease results in remodeling and narrowing of the arteries that supply oxygenated blood to the heart, and thus may lead to myocardial infarction. Common interventional approaches include percutaneous coronary intervention and coronary artery bypass graft surgery (American Heart Association, 2017). The choice of treatment will vary depending on a range of clinical factors, including morphology of the vessel wall, and degree of stenosis as quantified by cross-sectional luminal area.

In percutaneous coronary intervention, various imaging modalities can be used to assess coronary artery disease. One of these methods is intravascular optical coherence tomography (IVOCT). Using this imaging modality, in vivo rotary pullback imaging of human coronary arteries are performed whereby the optical fiber core in the catheter, which is positioned within the coronary lumen, undergoes rotation and translation to generate a sequence of images depicting internal structure of the arteries. The rotary pullback images acquired subsequently undergo image segmentation for analysis. The analysis is important to quantify the mechanism and nature of coronary artery diseases and identify the most appropriate treatment methods.

1.1 Problem statements

One of the features of interest that can be extracted from IVOCT image is the coronary lumen. Delineation of the vessel lumen in IVOCT images enables quantification of the luminal cross-sectional area. Such delineation has also been used as the first step towards plaque segmentation (Bengio, Goodfellow, & Courville, 2015; Celi & Berti, 2014) and the assessment of stent apposition (Adriaenssens et al., 2014). However, manual delineation is impractical due to the high number of cross-sectional

scans acquired in a single IVOCT pullback scan, typically >100 images. Automatic delineation of the lumen wall is challenging for various reasons. Non-homogenous intensity, blood residue, the presence and absence of different types of stents, irregular lumen shapes, image artifacts, and bifurcations are some of these challenges (Guillermo J. Tearney et al., 2012).

1.2 Objectives

The main objectives of this study are

- to facilitate quantitative assessment of coronary artery stenosis and stent placement by developing a fully automatic segmentation framework to extract coronary lumen from optical coherence tomography images.
- to investigate the feasibility and performance of using the linear-regression CNN to segment lumen of the coronary arteries for facilitating stenosis grading
- to provide a more accurate and robust segmentation of lumen for coronary artery disease diagnosis in wide spectrum of clinical OCT

In this study, a novel method of coronary lumen segmentation using a linear-regression convolutional neural network (CNN) was proposed. The algorithm was tested on in vivo clinical images and assessed against gold-standard manual segmentation. This is the first use of a linear-regression CNN approach to the automated delineation of the vessel lumen in IVOCT images.

1.3 Thesis Outline

This thesis is organized as follows: in Chapter 1, the general overview, problems, objectives and study proposal were presented; in Chapter 2, the background and review previous works by other researchers related to the field of study, methods and

techniques were described; in Chapter 3, methodology employed to develop and implement a linear-regression convolutional neural network was described; in Chapter 4, the results and statistics of our neural network training and predictions, benchmarked against interobserver variability of manual segmentation were presented; in Chapter 5, the discussions pertaining to the results obtained, potential clinical impact and limitations of such approach were elaborated; and lastly, in Chapter 6, the conclusions of the study were stated and the potential future work was briefly described.

University of Malaya

CHAPTER 2: LITERATURE REVIEW

2.1 Cardiovascular disease and Coronary Artery Disease

Cardiovascular disease, more commonly known as heart disease is attributed as the global leading cause of death for both men and women according to the World Health Organization (WHO) (World Health Organization, 2014).

Coronary artery disease, a variant of cardiovascular disease, is defined as the narrowing of the blood vessels that supply oxygenated blood to the heart. Such narrowing is also known as stenosis. Stenosis is caused by atherosclerosis, resulting from the formation of a plaque within the vessel. Plaques are build-ups of various biological components which include fatty tissues, cholesterol, calcium, macrophages and smooth muscle cells. Atherosclerotic plaques can be histologically classified into fibrous, fibro-calcific and lipid-rich (Yabushita et al., 2002). Vulnerable plaques are plaques with high tendency to rupture and cause a massive thrombosis leading to a myocardial infarct or a heart attack (Castelli, 1998). These vulnerable plaques are usually lipid-rich and lack support components to hold its cellular components. The determination of plaque vulnerability is based on the core size of the plaque, cap thickness, and cap inflammation and repair (Kristensen, Ravn, & Falk, 1997).

Treatment options vary depending on the necessity and severity of the disease. Some treatment options for coronary artery disease are percutaneous coronary intervention (PCI) which is more commonly known as angioplasty, and coronary artery bypass graft surgery (American Heart Association, 2017). In PCI, a stent is inserted into the narrowed region of the artery. Stents are mesh tubes inserted into the blood vessel to sustain an opening in a previously obstructed passage, which in this case is the artery. Coronary artery bypass grafting is a medical procedure that uses grafts, i.e. vessels from other parts of the body, to create an alternative passageway for blood flow around the blocked artery. PCI has some advantages over bypass graft surgery. PCI is considered

less invasive, has shorter procedure duration and usually requires only an overnight stay at the hospital. In contrast, bypass graft surgery is more invasive as it requires arteries or veins from other parts of the body and the number of bypass is determined by the number of blocked coronary arteries as well as requiring a longer stay in the hospital. Nevertheless, these treatments are aimed to improve blood flow through blocked artery, to reduce the risk of heart attack and to improve the ability for an individual for physical activity.

The diagnosis and assessment for the treatment of coronary artery disease are performed by clinicians or cardiologists using various medical technologies. The assessment involves the determination of plaque vulnerability in coronary artery disease. To qualitatively and quantitatively assess plaque vulnerability and coronary artery disease, different imaging modalities are used. This will be discussed in the following section.

2.2 Imaging modalities of coronary artery disease assessment

Imaging modalities are medical technologies employed by clinicians to aid in visualizing the interior of the body for diagnosis and treatment recommendation. There are various types of imaging modalities which are used for the visualization of coronary artery. These include X-ray angiography, computed tomography coronary angiography (CTA), cardiac magnetic angiography imaging (CMR) (Dowsley et al., 2013), intravascular ultrasound and intravascular optical coherence tomography.

2.2.1 X-ray angiography

The most commonly and widely accepted method for PCI is conventional X-ray angiography and it is considered the gold standard for the assessment of coronary artery disease (De Franco & Nissen, 2001). X-ray angiography produces a two-dimensional projection image of the contrast filled vessel. This modality requires the use of x-ray

radiation and contrast agent for vessel visualization. The images generated are in planar form with images of different arteries overlapping one another (Figure 2.1).

Despite being used as the predominant imaging modality, there are inherent limitations associated with X-ray angiography. These include the limited resolution and quality of imaging leading to the limited accuracy in assessing the volume of plaque build-up in the arteries. The limitation is associated with the mechanism of X-ray angiography whereby only the shape of the contrast-filled vessel lumen is visualized, excluding the imaging of the volume of plaque on vessel wall. This consequently limits detailed understanding of the disease morphology to support decision making process in diagnosis and treatment. Other limitations include the qualitative interpretation of X-ray angiography images which is subject to inter-observer variability, and the risks with the use of ionizing radiation (Budoff, Achenbach, & Duerinckx, 2003).



Figure 2.1: An image of a X-ray angiogram (Auricchio, Conti, Ferrazzano, & Sgueglia, 2014).

2.2.2 Computed tomography (CTA)

Computed tomography (CTA) is generally used to for anatomic assessment. Similar to X-ray angiography, CTA is able to show blockage of the arteries when a contrast agent is introduced into the arteries. CTA works by taking multiples images and

reconstruct them in three dimensions to evaluate the heart and coronary arteries. Due to its high sensitivity, it can be subjected to an overestimation in diagnosing stenosis with high calcium content. However, the major disadvantage of CTA is patient exposure to radiation and the use of iodinated contrast (Dowsley et al., 2013). In addition, this imaging modality is limited in terms of its ability to visualize plaque structure, volume and composition.

2.2.3 Cardiac Magnetic Resonance Imaging (CMR)

CMR is excellent to assess structural information of the artery. CMR also has 3D capabilities to allow assessment of coronary artery in various anatomical planes. However, CMR cannot be used in patients with recent stent placement in the artery (Budoff et al., 2003) or with a cardiac pacemaker implanted. The advantage of CMR is it does not use ionizing radiation. However, it is inferior in terms of imaging resolution as compared to CTA (Dowsley et al., 2013).

2.2.4 Intravascular Ultrasound (IVUS)

Another imaging modality used for the assessment of coronary artery disease is intravascular ultrasound (IVUS). IVUS is an invasive imaging modality whereby a catheter containing an ultrasound transducer is inserted into the artery. IVUS uses high frequency ultrasound to image the vessel wall and its internal structures including atheroma distribution, the compositions of plaque, and to assess vessel vascular response (De Franco & Nissen, 2001). Using IVUS, the three layers of the lumen wall, i.e. intima, media and adventitia can be visualized. In a normal coronary artery as shown in Figure 2.2(a), each layer is distinguished according to contrast of the bands displayed as seen in Figure 2.2(b). (De Franco & Nissen, 2001) also cited the advantages of IVUS compared to X-ray angiography, whereby IVUS is able to perform a 360° interior

visualization of the vessel wall layers, therefore the ability of IVUS to evaluate the severity of diseased atherosclerotic tissues in the coronary vessels. Furthermore, (Nissen, 2001) states that IVUS has better potential to identify vulnerable plaques and provide an approximate thickness of fibrous caps, as well as having the potential to visualize changes in plaque volume. IVUS has been used in complementary with X-ray angiography in clinical PCI to enhance the assessment of CAD.

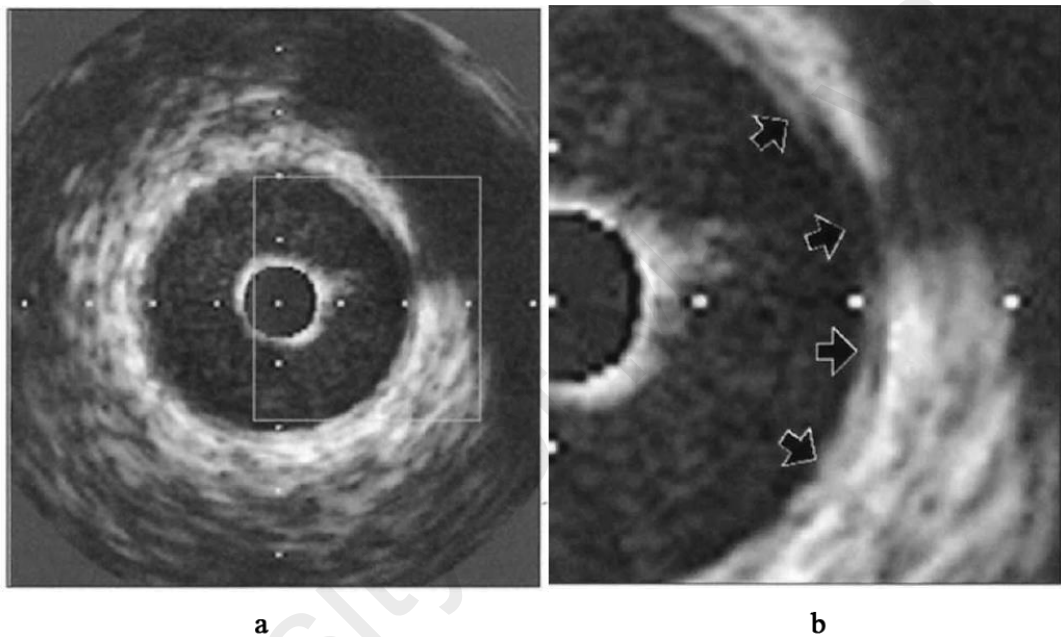


Figure 2.2: (a) Normal coronary artery visualized using IVUS. (b) A segment of showing layers of the coronary artery wall. The intima is the white stripe indicated by the black arrows. The media is indicated by the black sonolucent band beyond the intima. The adventitia is indicated by the bright white area beyond the media (De Franco & Nissen, 2001).

IVUS permits the measurement of lumen cross-sectional area, media-adventitia area, the maximum and minimum intimal thickness, and the percentage of narrowing in the vessel (De Franco & Nissen, 2001). However, there are some limitations in IVUS. IVUS is insufficient to image and diagnose certain vascular features in CAD such as thrombus, lipid pools, calcium, and fibrotic tissues due to its lower resolution (Prati et al., 2010). In addition, insertion of the catheter into the blood vessel has the potential to cause trauma to the vessel wall.

2.3 Optical coherence tomography

Intravascular OCT is an alternative imaging modality for plaque assessment which, like IVUS, is deployed through intravascular insertion of an imaging probe. The mechanism of how OCT captures the image is analogous to ultrasound, except that OCT uses near-infrared light, at a wavelength of approximately $1\mu\text{m}$, instead of sound waves. The cross-sectional images are two-dimensional (2D) and they are generated through low-coherence interferometry, which allows calculation of the level of optical backscatter at different depths in the internal tissues (Huang et al., 1991). In coronary artery OCT imaging, these internal tissues are the plaques and vessel wall.

OCT studies have shown that this modality has some advantages over IVUS. OCT has approximately 10 times higher imaging resolution of approximately $15 - 20\mu\text{m}$ compared to IVUS at approximately $100 - 200\mu\text{m}$. At this resolution scale, OCT is able to image the normal vessel wall as a layered architecture consisting of intima, media and adventitia (Figure 2.3), while IVUS could hardly distinguish the boundary of intima and media if the thickness of the intima is less than $180\mu\text{m}$. OCT also allows the detection of thrombus and differentiation between red and white thrombi (Mauri et al., 2005), although non-protruding red thrombi may be sometime mistaken for necrotic lipid pools at such resolution (Prati et al., 2010). OCT is superior to IVUS in classifying lipid plaques but is limited in total lipid pool area measurement due to the limited penetration depth of OCT (Kume et al., 2006). OCT has penetration depth of approximately $1-2.5\text{mm}$ as compared to IVUS which has penetration depth of approximately 10mm (Prati et al., 2010).

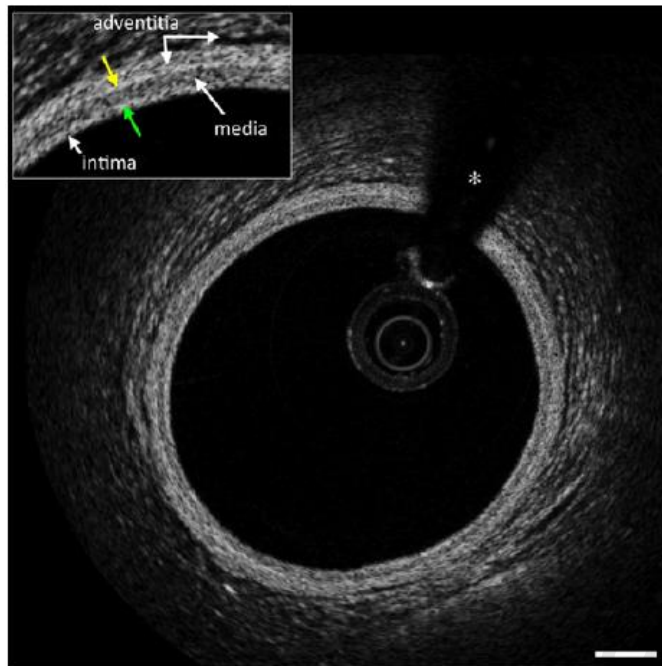


Figure 2.3: Normal artery wall comprising of the intima, media and adventitia visualized using intravascular OCT (Guillermo J. Tearney et al., 2012).

To carry out scanning, the light emitted from the laser source of the OCT system is separated into two optical paths. One is directed to the tissue through the sample arm while the other is directed to a predetermined distance and reflected back from a mirror in the reference arm. The light beams from both arms are subsequently combined and their interference allow for a calculation of the level of optical backscatter at different depths in the tissue. There are two main types of OCT systems: Time-Domain OCT (TD-OCT) and Fourier-Domain OCT (FD-OCT) as shown in Figure 2.4. In the TD-OCT system, a broadband light source is used and the distance travelled by light in the reference arm is mechanically scanned by a moving mirror for depth gating. In contrast, in swept-source OCT, which is a common implementation of FD-OCT, a fast-tunable laser source is used and the length of the reference path remains fixed. The level of optical back-scatter at different depths along the sample path for this system is calculated through the use of Fourier Transform (Bezerra, Costa, Guagliumi, Rollins, & Simon, 2009). Both systems have been used in OCT studies pertaining to coronary

artery disease. FD-OCT allows more rapid scanning, as it avoids the limitation of needing to physically move a mirror in the reference light beam path.

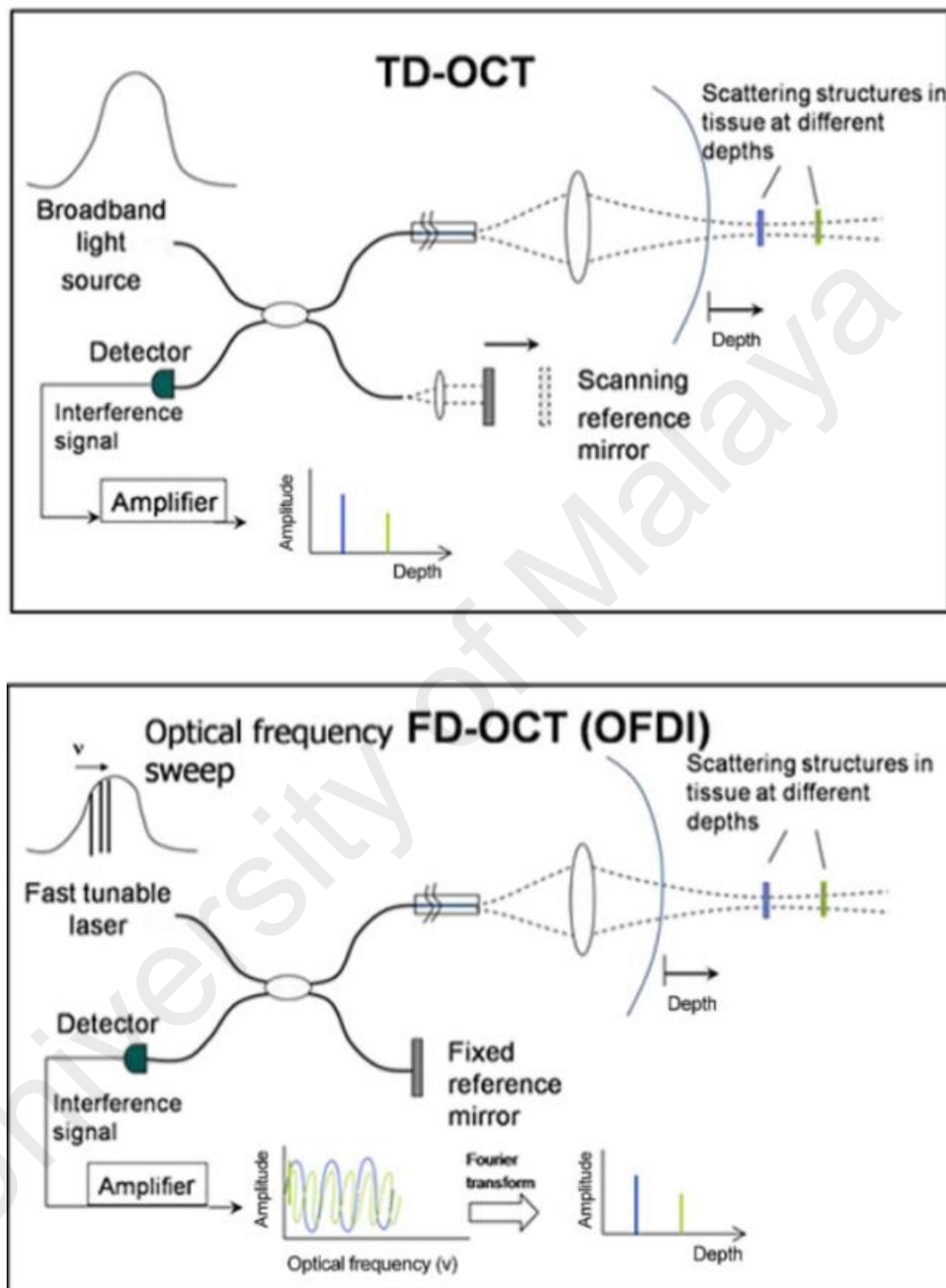


Figure 2.4: Scheme of TD-OCT (top) and FD-OCT (bottom). From (Bezerra et al., 2009)

Entire cross-sectional OCT images are acquired through a full revolution of a rotating imaging probe within the coronary artery, yielding multiple axial scans (A-lines) as seen in Figure 2.5. This image is also called a polar image, which is

represented in the polar coordinate system. A B-scan image is the cross-sectional image which is a rendering of the sequence of adjacent axial scans with a fixed reference point which is usually the center of the imaging probe encased within a catheter shown in Figure 2.5.

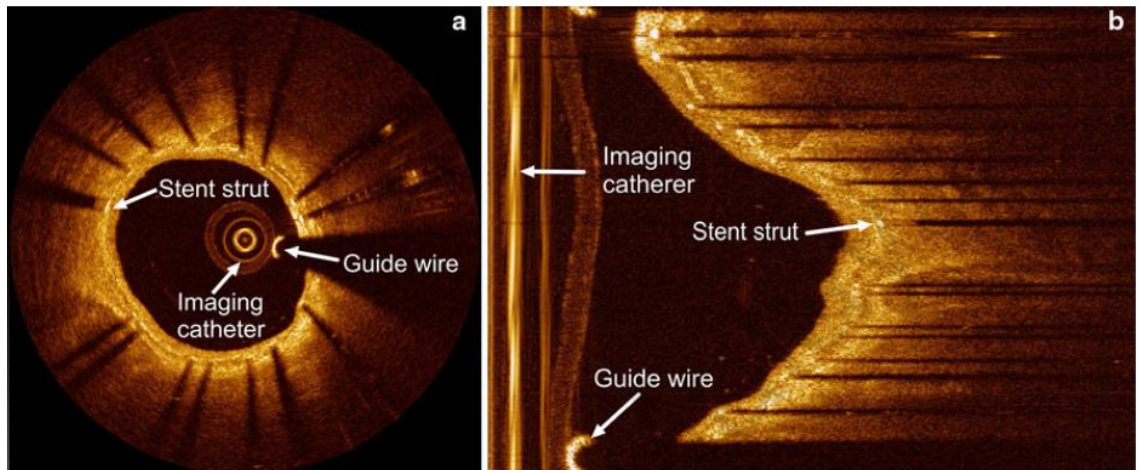


Figure 2.5: A B-scan (left) and an axial scan of an OCT image (right). From (Wang et al., 2013).

The interpretation of OCT images can be performed based on a standard compiled by the International Working Group for Intravascular OCT Standardization and Validation (Guillermo J. Tearney et al., 2012). This documentation compiles the standards for all characterization of various tissue features related to CAD, defines the qualitative properties of tissues, and defines the quantitative measurements for OCT image analysis.

Early studies performed by (Patwari et al., 2000) showed the ability of OCT to visualize coronary plaques present in the tissue of artery vessels at microscopic level. By analyzing tissue optical properties, OCT can be used to differentiate composition of plaques such as fibrous plaque, macro calcification, lipid pools and fibrous cap (Jang et al., 2002). The authors of this study compared the findings with histology and IVUS and concluded that OCT is capable of identifying most features detected by IVUS. (Kume et al., 2006) found that OCT had a higher sensitivity of 85% compared to 59% by IVUS in

characterizing lipid rich plaques. These works indicate the feasibility and ability of using OCT as an alternative to the methods available to assess CAD. However, the article also acknowledges the limitations and some disadvantages of OCT such as the limited tissue penetration which does not allow the accurate estimation of large plaque sizes.

OCT is also used in quantifying and visualizing in-stent restenosis post-stent implantation. Being able to do so is an important factor in understanding the mechanism of in-stent restenosis using drug-eluting stents and (Gonzalo et al., 2009) demonstrated the ability of OCT to delineate different patterns of restenotic tissues post-stenting. Their quantitative study involved parameters such as the length of stenotic segment, minimum lumen diameter and percentage measurement of stenosis while the qualitative study involves the classification of the types of restenosis tissues. OCT was shown to be able to visualize details of lumen shape and the components of the tissues in restenosis.

2.3.1 Segmentation of optical coherence tomography

Image segmentation is the process of extracting structures from an image, typically by labeling parts of the image into distinct categories. Features present in OCT images of coronary artery include atherosclerotic plaques, thrombus, stents and wall layers (Guillermo J. Tearney et al., 2012). Some clinically relevant measurements that are indicative of the severity of coronary disease and performed in coronary OCT segmentation includes lumen dimensions, area of coronary plaques, area of restenosis, and stent apposition measurements (Guillermo J. Tearney et al., 2012).

In current clinical application, manual assessments are employed by clinicians to assess OCT images of coronary artery disease cases. Assessment based on manual tracing by human experts to identify the features previously mentioned from slice to

slice is very time consuming and subject to inter-observer variability. Automatic segmentation, which uses algorithms designed to automatically extract the features of interest, is therefore desirable to aid segmentation of pullback scans consisting of hundreds of cross-sectional images during surgical operation.

Various methods have been developed to automatically delineate features in the coronary vessel wall, including the lumen, which is assessed when attempting to quantify the extent of stenosis by means of the luminal area (Celi & Berti, 2014; Gonzalo et al., 2009). (Kai-Pin, Wen-Zhe, De Silva, Edwards, & Rueckert, 2011) performed a study on lumen segmentation from IVOCT images using a combination of Expectation-Maximization (EM) and graph-cut based segmentation algorithms. Their method initially clustered the image pixels based on K-means, followed by processing them through an Expectation-Maximization (EM) algorithm to generate Gaussian mixture models used to threshold the intensity values. Once the image was thresholded, a graph-cut algorithm was implemented to estimate the boundary of the vessel wall. Graph-cut algorithm performs segmentation based on the minimization of energy function and a foreground or background label is assigned to each pixel (Boykov & Jolly, 2001). The guide wire shadow artifacts were subsequently removed using a convex hull approach, and the lumen border contour was corrected and smoothed using active contours.

(Celi & Berti, 2014) developed a semi-automated method to perform in-vivo quantitative analysis of the plaque components by employing two groups of hierarchical flow in searching for the desired region of the vessel tissue shown in Figure 2.6. Each hierarchical flow contains a series of systematic steps that the images undergo. Their approach provides segmentation of the lumen, fibrous plaques, fibro-calcific plaques, and lipid plaques. For their lumen segmentation, a set of radial lines were projected

from the center of the catheter outwards on a binary OCT image previously threshold using the Otsu's method (Otsu, 1975). The vessel lumen boundary is determined at the intersection points of the radial lines and the boundary of the binary image between the lumen and vessel tissue. These points are then smoothed and connected using a Savitzky-Golay filter resulting in a lumen vessel contour. The Savitzky-Golay filter works by smoothing out noisy signals through polynomial regression. Fibrous plaques, by contrast, are determined using a decorrelation stretch and a median filter yielding a binary image by delineating signal-rich homogeneous areas. Fibro-calcific plaques are segmented semi-automatically, with the user manually inputting the region to search. The calcific region is then defined as the subtraction of convex hull of the fibrous region of the tissue with the areas of lumen and fibrotic tissue. Lastly, lipid plaques are automatically segmented based on homogenous low-signal intensity regions. Tissue measurements were performed by calculating the difference between the pair of points of the A-lines.

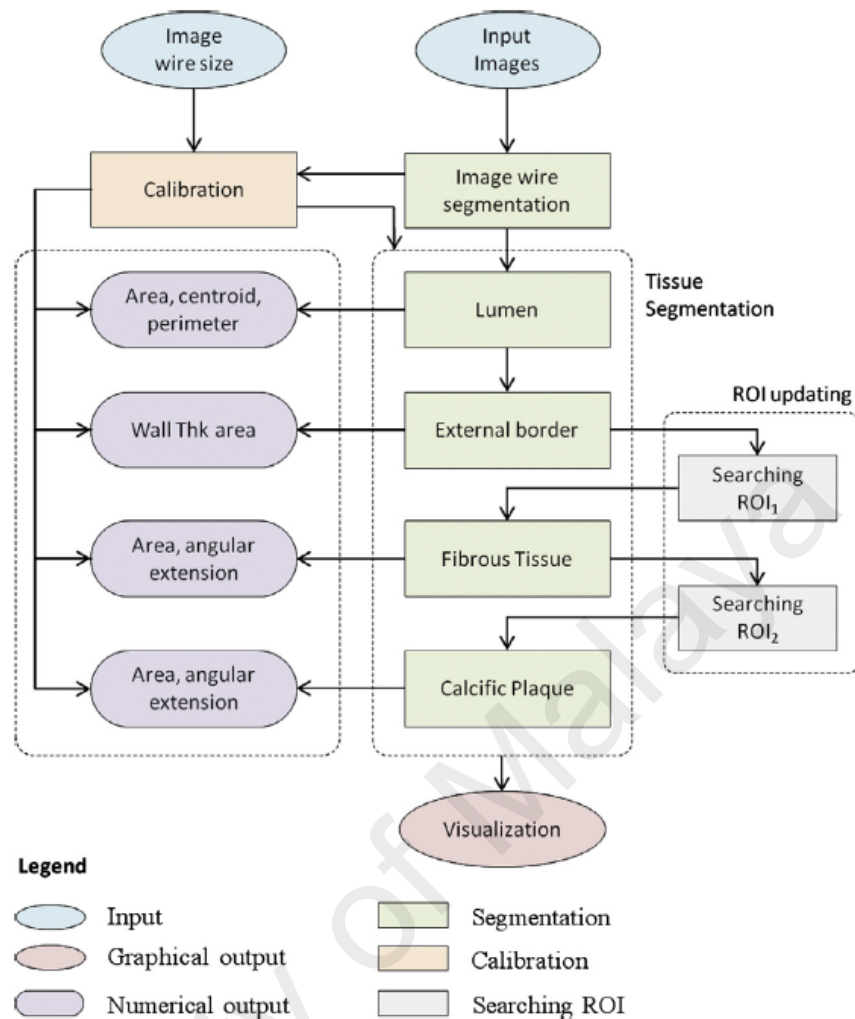


Figure 2.6: Image processing framework proposed by (Celi & Berti, 2014).

Mathematical splines have also been used in the development of automated OCT segmentation. Splines are piecewise-defined polynomial functions. (Gurmeric, Isguder, Carlier, & Unal, 2009) defined the lumen segmentation by initializing and propagating a Catmull-Rom spline algorithm. Catmull-Rom spline is an interpolating spline with four polynomial blending functions defined by controls points located on the spline contour. The splines were initiated from the center of the image outwards to the lumen boundary and terminated using an edge-based active contour framework at the desired boundaries. This is part of their methodology to develop a three-dimensional automated computational method for in-stent neointimal hyperplasia.

Computer-aided segmentation has also been developed to detect stent struts from OCT images. Struts are the parts that form the framework of the stents. As described by (Guillermo J. Tearney et al., 2012), stents, which are usually metal in nature, have an opaque property blocking the OCT light from passing through them yielding a shadow behind the strut. Pixel intensities and gradient of intensities of the OCT image have been used for detecting and segmenting stent struts by (Giovanni Jacopo Ughi et al., 2012) and (Wang et al., 2013). Both research groups developed their methods for such detection utilizing A-scan intensity profiles of the OCT images. The method by (Giovanni Jacopo Ughi et al., 2012) measures the apposition of the metal stents with the vessel wall while the study by (Wang et al., 2013) focuses only on metal stent detection. These two studies take the advantage of intensity profiles with relation to the bright spots and trailing shadow of the A-scans present in the image for the segmentation task.

Specifically, (Giovanni Jacopo Ughi et al., 2012) developed a semi-automatic algorithm to calculate the differences in intensity profiles of the A-lines of the OCT image based on a binary or a-priori input by a user to determine the type of struts assessed which is either apposed or covered. Their goal was to evaluate the stent strut apposition and neointimal coverage post-stenting. This method uses the gradient of the intensity profile of the bright pixels of the struts against the trailing dark region of the shadow. As such, the authors classified each intensity profile into four different properties that would be quantified: 1) intensity of peak from each A-line, 2) the presence of shadow, 3) the length of the shadow, and 4) the rate of change of rise and fall of energy as a function of depth. Based on these properties, the A-lines are classified either to contain a strut candidate or a region with tissue based on the pixel intensity gradient computed based on a certain threshold.

(Wang et al., 2013) demonstrated a similar approach, using intensity gradient to calculate the intensity profiles. The authors of that study employed a shadow detection method to determine the edges of the trailing shadow of the struts using kernels and clustering of candidate pixels. However, the method of clustering the pixels of the shadow edge can be prone to false positives such as detecting the shadow of the guidewire, although this can be reduced by careful selection of threshold values. Clustering algorithms, such as those used in that work, also can have issues as image quality varies. Clustering algorithms will typically define clusters so as to minimize the squared Euclidean distance between the data points and the cluster centers. The limitation of this method is when there is little to no trailing shadow behind the struts making it impossible for the algorithm to detect. In addition, this method is not feasible in cases of low quality images with a trailing shadow and the absence of bright spots. Methods by both (Wang et al., 2013) and (Giovanni Jacopo Ughi et al., 2012) therefore may work well on the task of segmenting metal stent struts. However, the techniques are unlikely to work on bioresorbable stent struts which neither appears as bright spots in the image nor causes trailing shadow.

(G. J. Tearney et al., 2003) demonstrated that OCT is capable of quantifying the high intensity signal in fibrous cap which could potentially be rich with macrophages. The study was performed on cadavers with co-registration to histology. (Phipps et al., 2015) developed an algorithm to quantify these areas of high intensity and compare against histological examination. Normally, areas of high backscatter in intravascular OCT are usually associated to stents struts (Giovanni Jacopo Ughi et al., 2012; Wang et al., 2013) or the regions close to lumen vessel boundary. The intensity diminishes deeper into the tissue. Therefore, (Phipps et al., 2015) plotted a graph of A-scan intensities against tissue depth. Any plot of pixel intensity that is outside of the region of the stents and is deeper in the vessel tissue than the blood-tissue boundary has a higher probability to be

labeled as macrophage-rich plaque. The results were compared with histology examination and four different statistical analyses were performed by expert IVOCT readers. Their results indicated macrophages was present in 23% of the high backscatter regions. (Phipps et al., 2015) concluded that not all regions of high backscatter are caused by macrophages and that a better algorithm development is required.

Several studies (De Cock, Tu, Ughi, & Adriaenssens, 2014; Slager et al., 2000; Guillermo J. Tearney et al., 2008) have proposed the value of performing segmentation on 3D OCT data sets. The validation methods by the studies discussed included manual human assessment, which is considered a standard procedure (Celi & Berti, 2014; Kai-Pin et al., 2011; Phipps et al., 2015; Giovanni Jacopo Ughi et al., 2012; Wang et al., 2013) and some with histology examination (Phipps et al., 2015; G. J. Tearney et al., 2003). Phantom validation can be used but there is a limitation in this method as it lacks standardized phantoms that can be used as a reference (Celi & Berti, 2014).

In terms of lumen segmentation involving IVOCT images, there have been very limited studies that focus on the segmentation of pre-stented lumens. In addition, there is no robust study that has shown the feasibility of a segmentation algorithm to perform pre- and post-stented segmentation. The post-stenting assessment is crucial in PCI assessment as these images could provide vital information on the quality of stent placements and the amount of restenosis during follow-up scans. Therefore, this has motivated the current research to explore robust algorithms to segment the extensive variations of lumens in IVOCT images acquired in a real clinical setting.

2.4 Neural networks

Artificial neural networks (ANN) are a mathematical model inspired by neurons in the human brain, in terms of how they organize and relay information to generate a

certain output. A neural network model generates a non-linear function based on a set of training examples. Given a training set, an artificial neural network algorithm is able to learn to fit a set of derived parameters. The general structure of a neural network is composed of multiple layers, including an input layer, hidden layers and an output layer. The number of hidden layers is user-defined and dependent on the complexity of the system (Amato et al., 2013). The more hidden layers there are, the more features that can be learned but usually with the cost of increased processing and computation time. A general artificial neural network is shown in Figure 2.7. Neural networks are capable of performing either binary or multiclass classifications.

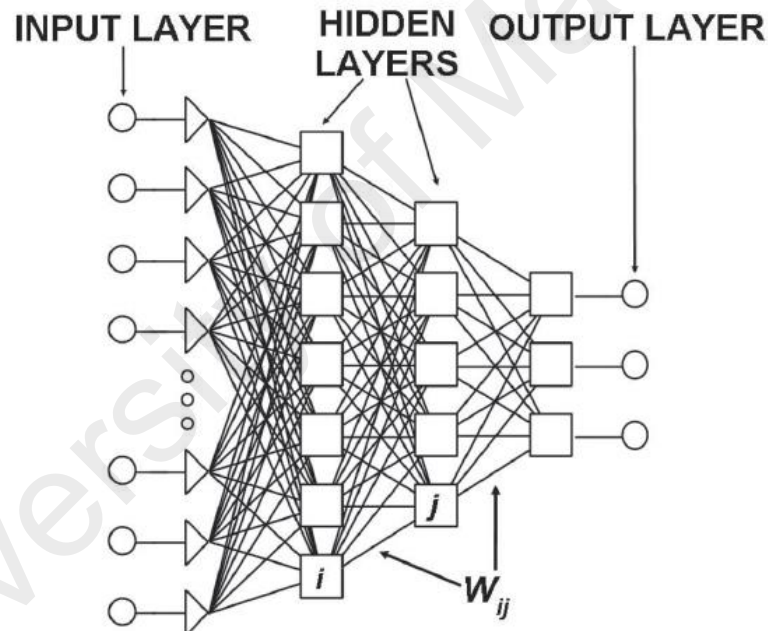


Figure 2.7: General structure of a neural network with two hidden layers. W_{ij} indicates the weights of the link between layers (Amato et al., 2013).

The general advantages of neural network are that they are capable of processing complex non-linear relationships; and are capable of detecting the relationships between all input variables. They can be developed using different training algorithms with the most common one being variants on the backpropagation algorithm (Tu, 1996).

Limitations of artificial neural network include that it is difficult to determine and identify causal relationship; and that inaccuracies may arise due to over fitting (Tu, 1996). Over fitting is prone to occur if training sample size is too small or prediction is performed on data set with characteristics vastly different from the training set.

2.4.1 Background and intuition of neural networks

Deep learning is a type of machine learning algorithm utilizing artificial neural networks. The general process how an ANN works is by processing input features through a multi-layered network. This network is parameterized by a collection of weights and biases. Weights and biases are sets of learnable values that dictate the mapping from layer to layer. These weights and bias values are optimized by minimizing a loss function through a process called training. One common loss function used is the standard Mean Squared Error between the desired output and the current output for a given training input. Mathematically, the loss function in neural networks can be described as follow (Eq(2.1)):

$$\text{MSE}_{train} = \frac{1}{N} \sum_{i=1}^n (\hat{y}_{train} - y_{train})^2, \quad \text{Eq (2.1)}$$

where $\frac{1}{N} \sum_{i=1}^n$ is the mean, \hat{y} is the desired output, and y is the predicted output.

The partial derivatives of the loss function with respect to the parameters of the network are then determined and accumulated. In each iteration, the parameters are changed such that the improvement in the loss function is maximized using gradient descent algorithm. Through this process, the training inputs are mapped to known target output values. This process is repeated until convergence, i.e. a desired minimal loss value is obtained.

Convolutional neural networks (CNN) work similarly to a traditional ANN except that convolutional filters are applied to the input of each layer instead of a general matrix multiplication (Goodfellow, Bengio, & Courville, 2016). Each layer that is convolved by the convolutional filters is known as the convolutional layers. The convolutional filters, also known as kernels, serve to extract features from input by sliding across the input with a pre-determined stride. Stride is the distance the filter is being translated over a particular input vector. As it moves over an area, it performs the convolution operation of the information within filter's area. Since a filter has a pre-determined size, padding of pixels valued at zero can be added to allow the filter to include the information located at the boundary of an input.

Since convolutional filters yield linear outputs, some form of non-linearity has to be introduced. This is accomplished in the activation layers step and exponential linear units (ELUs) are one type of activation functions that could be applied (Clevert, Unterthiner, & Hochreiter, 2015). The use of ELUs is to address the vanishing gradient problem that can arise in achieving the desired minimal value in gradient descent. As the gradient reaches the minimal point, the slope becomes smaller and can result in very slow learning of weights. Vanishing gradient is a problem presented if other activation functions such as the tanh or sigmoid activation functions are used. ELUs can speed up the learning process during training.

Pooling can also be introduced into the network to subsample the inputs so that they are more manageable and makes the network identify representations that are invariant to small translations (Goodfellow et al., 2016). This means that the network is still able to identify features that differ slightly at a lower computational cost through learning of subsampled inputs. Even with the reduced image information, with pooling, the best representation of the input information is retained. One common example would be

Max Pooling. This method takes a filter of a determined size, usually 2x2 and downsample the particular region by taking the maximum value within the rectangular convolved filter to be output. After pooling, the process of passing through a new convolutional filter can either be performed again or the inputs are passed to the fully connected layers, which have the architecture similar to a generic neural network and contain the weights and biases as parameters to be optimized during training.

With the ability to recognize patterns in a set of data, neural networks have been used to predict coronary artery stenosis (Mobley, Schechter, Moore, McKee, & Eichner, 2000) and to detect blood vessels in angiograms (Nekovei & Ying, 1995). Both studies utilized a three-layer conventional generic neural network rather than the more advanced, newly emerging convolutional neural network.

2.5 Optical coherence tomography and convolutional neural networks

Convolutional neural networks have been utilized in image segmentation tasks in both medical and non-medical fields. In the medical field, deep-learning methods have been used to automatically segment OCT images of macular edema in human eyes (Lee et al., 2017). Their method applies the learning mechanism of CNNs to detect intraretinal fluid on 1289 OCT images. In other retinal OCT studies, deep learning has also been used to perform segmentation tasks such as segmenting foveal microvasculature (Bengio et al., 2015) and retinal layers (Fang et al., 2017).

In other medical fields, deep learning was used to segment brain tumor using the 2013 BRATS test data-set (Havaei et al., 2017). The segmentation was performed using a CNN architecture that accounts for both local features and global contextual features simultaneously. CNN was also used to classify lung image patches in interstitial lung disease (Li et al., 2014), head and lung cancer using hyperspectral imaging (LeCun, Bottou, Bengio, & Haffner, 1998), and arterial segmentation in patients with Kawasaki

disease (Abdolmanafi, Duong, Dahdah, & Cheriet, 2017). However, all these image segmentation tasks performed segmentation using CNN through feature classification approach, where the network is trained to classify each pixel in the input image into one of several classes.

Alternatively, instead of a feature classification approach, a regression approach can be used to train the neural network. A recent study utilizing linear-regression CNN was shown to outperform conventional CNN classification approaches in left ventricle segmentation (Tan, Liew, Lim, & McLaughlin, 2017). In this study, the radial distances between the left ventricle centrepoint and the endo- and epicardial contours in polar spaces were inferred using linear regression CNN.

2.6 Summary

Currently, CNN has already been used to segment tissue in coronary arteries but via feature classification approach (Abdolmanafi et al., 2017). Segmentation of lumen from OCT images has neither been demonstrated via CNN approach nor using the linear-regression CNN model. Therefore, this research aims to investigate the feasibility and performance of using the linear-regression CNN to segment lumen of the coronary arteries for facilitating stenosis grading. This method could potentially provide more accurate and robust segmentation of lumen for coronary artery disease diagnosis in wide spectrum of clinical OCT images as compared to published methods.

CHAPTER 3: METHODOLOGY

3.1 IVOCT data acquisition and preparation for training and testing

The data used for this study comprises IVOCT-acquired images of patients diagnosed with coronary artery disease. The IVOCT images were acquired from the University of Malaya Medical Center (UMMC) catheterization laboratory using two standard clinical systems: Illumien and Illumien Optis IVOCT Systems (St. Jude Medical, USA). Both systems have an axial resolution of 15 μm and a scan diameter of 10 mm. The Illumien system and the Illumien Optis system have maximum frame rates of 100 fps and 180 fps, respectively. The study was approved by the University of Malaya Medical Ethics Committee (Ref: 20158-1554), and all patient data were anonymized.

In total 64 pullbacks were acquired from 28 patients (25%/75% male/female, with mean age 59.71 (± 9.61) years) using DragonflyTM Duo Imaging Catheter with 2.7 F crossing profile when the artery was under contrast flushing (Iopamiro[®] 370). The internal rotating fiber optic imaging core performed rotational motorized pullback scans for a length of 54 mm or 75 mm in under 5 sec. These scans include multiple pre- and post-stented images of the coronary artery at different locations. These pullbacks were randomly assigned to one of two groups with a ratio of 7:3, i.e. 45 pullbacks were randomly designated as training sets and the remaining 19 as test sets. Excluding images depicting only the guide catheter, each pullback contains between 155 to 375 polar images. These images contain a heterogeneous mix of images with the absence or presence of stent struts (metal stents or bioresorbable stents or both), fibrous plaques, calcified plaques, lipid-rich plaques, ruptured plaques, thrombus, dissections, motion artifacts, bifurcations and blood artifacts. The original size of each pullback frame was 984×496 pixels (axial \times angular dimension), and was subsampled in both dimensions to 488×248 pixels to reduce training and processing time. For each image, raw

intensity values were converted from linear scale to logarithmic scale before normalizing by mean and standard deviation.

Gold-standard segmentations were generated on both training and test sets by manual frame-by-frame delineation using ImageJ (Schindelin, Rueden, Hiner, & Eliceiri) in Cartesian coordinates, according to the document of consensus (Guillermo J. Tearney et al., 2012), whereby a contour was drawn between the lumen and the leading edge of the intima. The contour was also manually drawn across the guidewire shadow and bifurcation at locations that best represent the underlying border of the main lumen, gauged by the adjacent slices. The manual contour of the lumen border for each image was subsequently converted to polar coordinates, smoothed and interpolated to 100 points using cubic B-spline interpolation method for CNN training and testing.

3.2 CNN regression architecture & implementation details

Using linear-regression CNN model, in each polar image the radius parameter of the vessel wall was inferred at 100 equidistant radial locations, rather than the more conventional approach of classifying each pixel within the image. This has the advantage of avoiding the physiologically unrealistic results that may arise from segmentation of individual pixels. The lumen segmentation was parameterized in terms of radial distances from the center of the catheter in polar space.

The general flow of the proposed CNN model is illustrated in Figure 3.1. Our network consists of a simple structure with 4 convolutional layers and 3 fully-connected layers, including the final output layer. All polar images were padded circularly left and right before being windowed for input. The window dimension was 488×128 pixels centered on each individual radial point, therefore yielding 100 inputs and 100 evaluated radial distances per image.

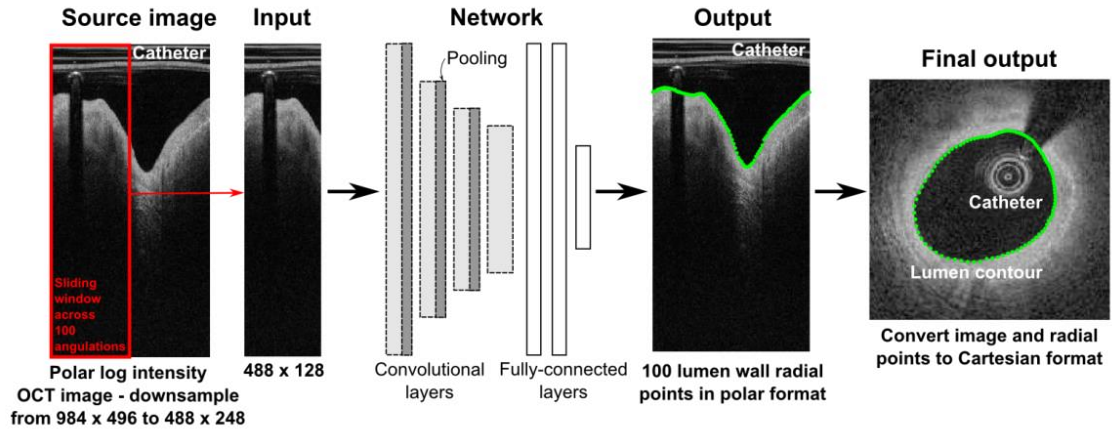


Figure 3.1: Overview of the linear-regression CNN segmentation system (refer to text for details).

The details of the network architecture are described in Table 3.1. In the network architecture, a filter kernel of size $5 \times 5 \times 24$ with boundary zero-padding was applied for all convolutional layers, yielding 24 feature maps at each layer. In the first layer, a stride of 2 was also applied along the angular dimension to reduce computational load. The first three layers were also max-pooled by size 2×2 . Each fully-connected layer contains 512 nodes. Exponential linear units (ELU) (Clevert et al., 2015) were used as the activation functions for all layers, including both convolutional and fully-connected layers, except the final layer. Dropout with keep probability of 0.75 was applied to the fully-connected layers FC1 and FC2, to improve the robustness of the network (Rokach & Maimon, 2005). The final layer outputs a single value representative of the radial distance between the lumen border and the center of the catheter for the radial position being evaluated.

The objective function used for the network training is the standard mean-squared error. Starting from a random initialization, the weight and bias parameters are iteratively minimized by calculating the mean squared error between the gold standard radial distance and the output of the CNN training. The Adam stochastic gradient algorithm was used to perform the optimization, i.e. minimization, of the objective

Table 3.1: Linear-regression CNN architecture for lumen segmentation at each windowed image. The output is the radial distance at the lumen border from the center of the catheter. CN: convolutional layer, FC: fully-connected layer.

Layer	In	Weights	Pooling	Out
CN1*	488×128×1	1×5×5×24	2×2	244×32×24
CN2	244×32×24	24×5×5×24	2×2	122×16×24
CN3	122×16×24	24×5×5×24	2×2	61×8×24
CN4	61×8×24	24×5×5×24	-	61×8×24
FC1	11712	11712×512	-	512
FC2	512	512×512	-	512
Out	512	512×1		1

*A stride of size 2 was applied on the angular dimension to reduce computational load

function (Kingma & Ba, 2014). The network was trained stochastically with a mini-batch size of 100 at a base-learning rate of 0.005. The base learning rate was determined empirically (refer to Appendix A)(Bengio et al., 2015). The learning rate was halved every 50,000 runs. The training was stopped at 400,000 runs where convergence was observed (i.e. when the observed losses had ceased to improve for at least 100,000 runs). The trained weights and biases of the network, amounting to approximately 6.3 million parameters, are subsequently used to predict the lumen contour on the test sets.

The neural network was designed in a Python (Python Software Foundation, Delaware, USA) environment using the TensorFlow v1.0.1 machine learning framework (Google Inc., California, USA). The execution of the network was performed on a Linux-based Intel i5-6500 CPU workstation with NVIDIA GeForce GTX1080 8GB GPU. The training time for 45 train sets was 13.8 hours and the complete inference time for each test image was 40.6 ms.

3.3 Validation

The accuracy of our proposed linear-regression CNN lumen segmentation was validated against the gold standard segmentation of the test data pullback acquisitions,

which were the aforementioned 19 manually delineated pullbacks. These pullbacks contain in total 5685 images. The accuracy was assessed in three ways: (1) on a point-by-point basis via distance error measure; (2) in the form of binary image overlaps and (3) based on luminal area.

The first assessment involves point-by-point analysis on the 100 equidistant radial contour points from all images, whereby the mean absolute Euclidean distance error between the gold standard and predicted contours was computed for each image.

The second assessment was performed to evaluate the regions delineated as lumen. The amount of overlap between the binary masks as generated from the predicted contours and the corresponding gold standards were computed using the Dice coefficient and Jaccard similarity index.

The third assessment targeted at the luminal area, which is one of the clinical indices to locate and grade the extent of coronary stenosis for treatment planning. Luminal area was computed from the binary mask produced from the predicted contours and compared against the corresponding gold standard. A 1-tailed Wilcoxon signed ranks test was also performed on the errors of the estimated luminal areas at significance level of 0.001. Three-dimensional surface models of the lumen wall were also generated for all pullbacks to facilitate visual comparison of the segmentation by manual contouring and by automated contouring using the proposed CNN regression model.

3.4 Dependency of network performance on training data quantity

To understand the dependency of the network performance to the amount of training data required, the variation in accuracy of the 19 test pullbacks was assessed against different numbers of training data sets. Tests were performed with 10, 15, 20, 25, 30, 35, 40 and 45 pullbacks. The training pullbacks for each group were selected randomly.

The number of training runs with different training sets was kept constant at 400,000 runs, with a similar base learning rate and learning rate decay protocol.

3.5 Inter-observer variability against CNN accuracy

To quantify the allowable variation in segmentation, an experiment to assess variation in the manual gold standard was performed that would be generated by three independent observers.

One hundred images were selected randomly from five pullbacks of the test sets and the lumen manually delineated by three independent observers. The interobserver variability was assessed through Bland-Altman analyses, consistent with Celi and Berti in their study on the segmentation of coronary lesions (Celi & Berti, 2014). Specifically, the signed differences between all possible corresponding pairs of luminal areas from all three observers were plotted against their mean area differences. Bland-Altman analyses were also performed on luminal areas evaluated by the CNN against the corresponding evaluation by all observers. These analyses provide an understanding of the total bias and limits of agreement (i.e. 95% confidence interval or $1.96 \times$ standard deviation of the signed differences from the mean) among all observers themselves as well as between the CNN and the observers.

CHAPTER 4: RESULTS

4.1 Dependency of network performance on training data quantity

The results assessing the impact of training data quantity on CNN accuracy are shown in Figure 4.1. The value reported here is the mean positional accuracy of each point along the vessel wall. There was notable improvement in CNN accuracy with increases in the training data quantity up until 25 training data sets. Beyond that, the mean absolute error per image varied little with increased data. However, the optimal CNN segmentation was obtained from training with the highest sample size, i.e. 45 pullbacks consisting of 13,342 training images, as summarized in Table 4.1. At 45 training pullbacks, the median of the mean absolute error per image as quantified using point-by-point analysis was 21.87 microns, whereas Dice coefficient and Jaccard similarity index were calculated as 0.985 and 0.970, respectively.

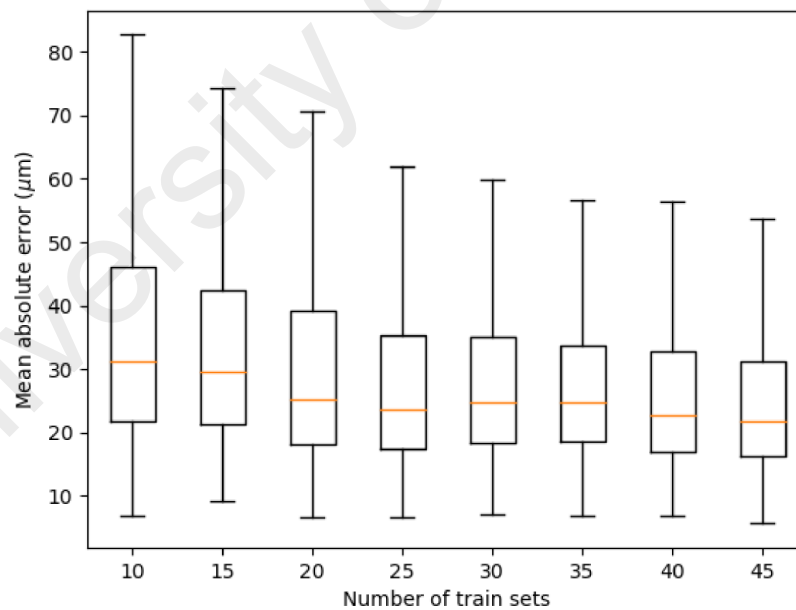


Figure 4.1: Mean absolute error against different numbers of training data sets.

Table 4.1: Accuracy of CNN segmentation with 45 training pullbacks (n = 13,342). The values are obtained based on the segmentation on 19 test pullbacks (n = 5,685).

Measure	Median (Interquartile range)
Mean absolute error per image (point-by-point analysis), μm	21.87 (16.28, 31.29)
Dice coefficient	0.985 (0.979, 0.988)
Jaccard similarity index	0.970 (0.958, 0.977)

Representative segmentation results are shown in Figure 4.2. Apart from performing well on images with clear lumen border contrast Figure 4.2(a), linear-regression CNN segmentation has shown robustness in segmenting images with inhomogenous lumen intensity (b), severe stenosis (c), blood residue due to suboptimal flushing (d)-(f), multiple reflections (g), embedded stent struts (h)-(i), malapposed metallic stent struts (j), malapposed bioresorbable stent struts (k), and minor side branches ((c), (i) & (l)). Acceptable lumen segmentation was found at the shadow behind the guide wire and metallic stent struts across all images. Errors were observed to occur most frequently at major bifurcations (angle spanning $>$ approximately 90°), where the appropriate boundary for segmenting the main vessel was ambiguous (Fig. 4.3 (c)-(d)). 72% of the 100 worst performing segmentation were found to contain major bifurcations and, at these locations, overestimation of the area of the main vessels was noted.

Based on the results obtained with the optimal training quantity (45 pullback data sets), the calculated luminal area estimates in all 19 test pullbacks, as tabulated in Table 4.2. CNN segmentation yields median (interquartile range) luminal area of 5.28 (3.88, 7.45) mm^2 matching well with the results of manual segmentation of 5.26 (3.93, 7.45) mm^2 (i.e. gold standard). The median (interquartile range) absolute error of luminal area was 1.38%, which is statistically significantly below 2% ($p < 0.001$) as tested by the 1-tailed Wilcoxon signed rank test. Figure 4.4 shows two representative examples of the 3D reconstructed vessel wall from two different pullbacks for visual comparison of

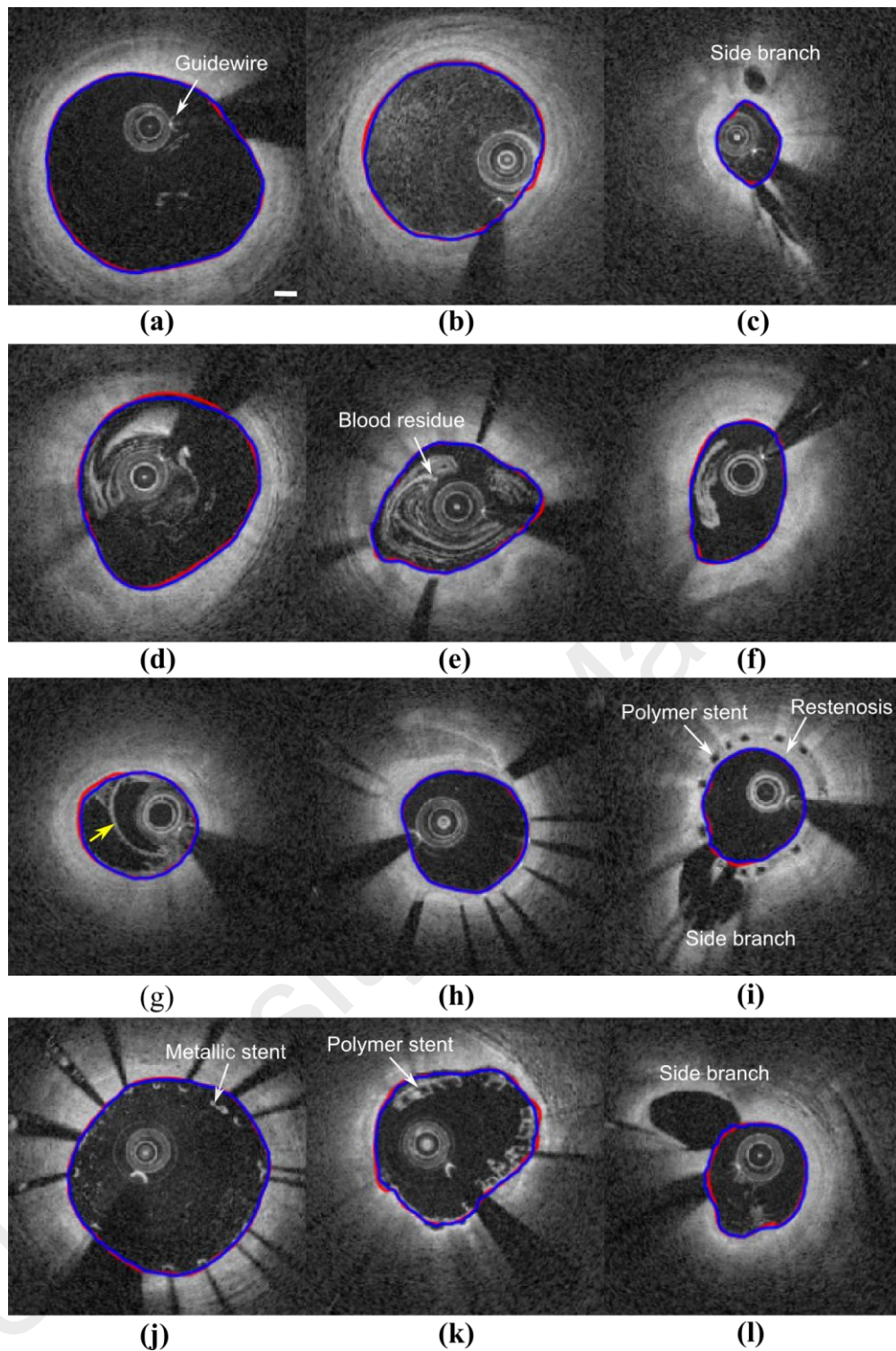


Figure 4.2: Representative results from the test sets, showing good segmentation from linear-regression CNN on images with good lumen border contrast (a), inhomogenous lumen intensity (b), severe stenosis (c), blood swirl due to inadequate flushing (d)-(f), multiple reflections (indicated by yellow arrow) (g), embedded metallic and bioresorbable stent struts due to restenosis in (h) & (i) respectively, malapposed metallic stent struts (j), malapposed bioresorbable stent strut (k), and minor side branch (l). Blue and red contours represent CNN segmentation and gold standard, respectively. Scale bar (a) represents 500 microns.

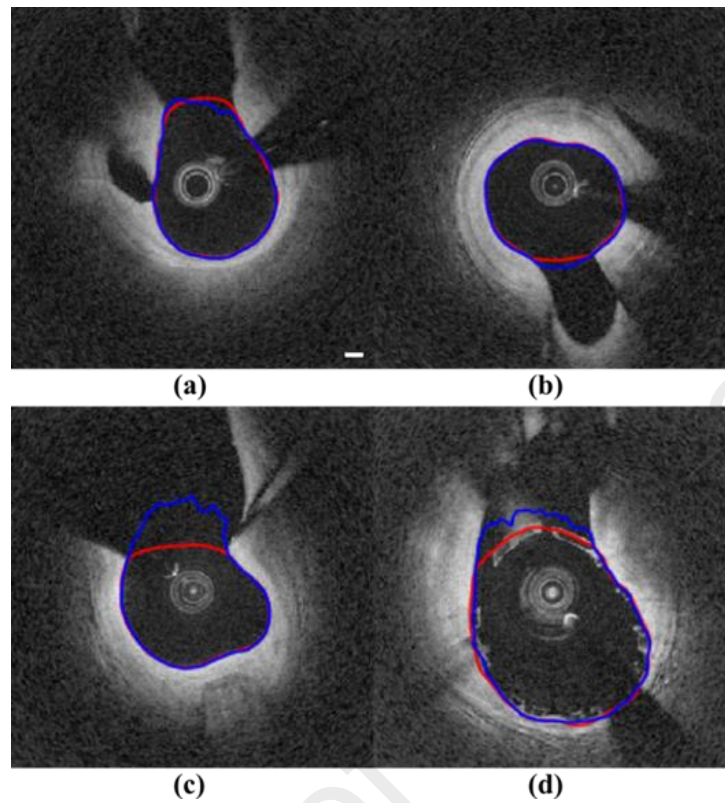


Figure 4.3: Representative cases from the test sets, showing reasonable lumen segmentation from linear-regression CNN on images with medium-sized bifurcations (a-b). Poorer results were seen at major bifurcations (c-d), where the appropriate boundary for segmenting the main vessel was ambiguous. Blue and red contours represent CNN segmentation and gold standard, respectively. Scale bar (a) represents 500 microns.

Table 4.2: Luminal area in 19 test pullbacks with optimal training

Method	Median (Interquartile range)
Luminal Area (mm²)	
Manual segmentation area	5.28 (3.88, 7.45)
CNN segmentation area	5.26 (3.93, 7.45)
Percentage Error^a (%)	
Signed percentage error	0.06 (-1.24, 1.53)
Absolute percentage error ^b	1.38 (0.63, 2.62)

^aNormalized by manual segmentation area

^bSignificantly below 2%, p<0.001

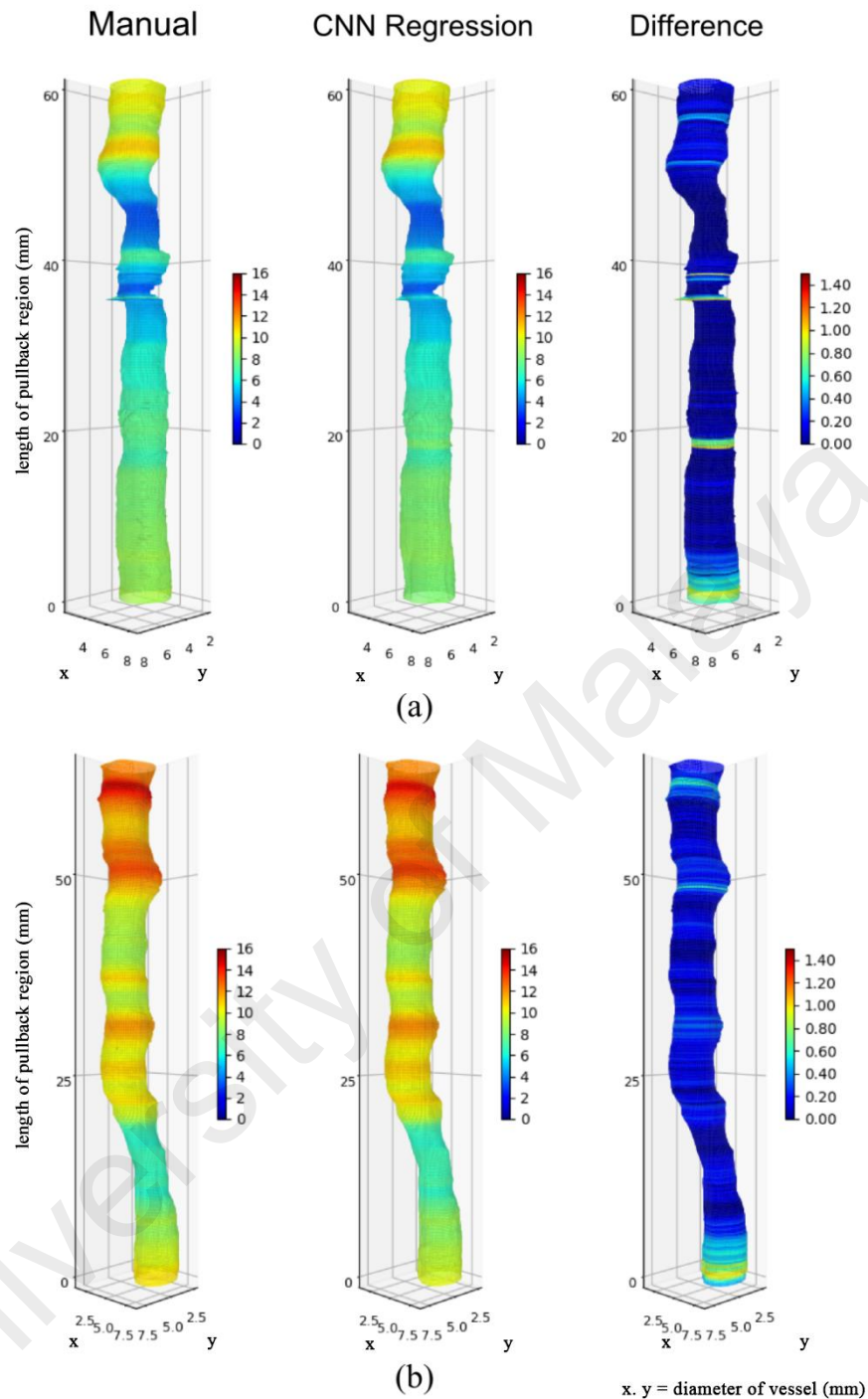


Figure 4.4: Reconstruction of vessel wall from two different pullbacks for visual comparison of CNN regression segmentation against the gold standard manual segmentation. Vessel walls (left and middle columns) are color-coded with cross-sectional luminal area. Difference in luminal area is displayed on the right. All the axis is in mm and colorbar indicates luminal area in mm^2 .

CNN regression (middle column) against gold standard manual (left column) segmentation. The vessel wall was color-coded with the cross-sectional luminal area.

Difference in luminal area between CNN regression and gold standard segmentation are color-coded on the vessel wall on the right column.

4.2 Inter-observer variability against CNN accuracy

The Bland-Altman analysis between all three observers showed a bias (mean signed difference) of 0.0 mm^2 and limits of agreement of $\pm 0.599 \text{ mm}^2$ in terms of luminal area estimation (Figure 4.5(a)). Comparing the CNN to all observers, the bias was 0.057 mm^2 and the variability in terms of limits of agreement was comparable at $\pm 0.665 \text{ mm}^2$ (Figure 4.5(b)). These results suggest that automated segmentation had sub-100 micron bias to over-estimate luminal area, and that the variation between automated and manual estimates of luminal area was only slightly greater than the inter-observer variability between human observers.

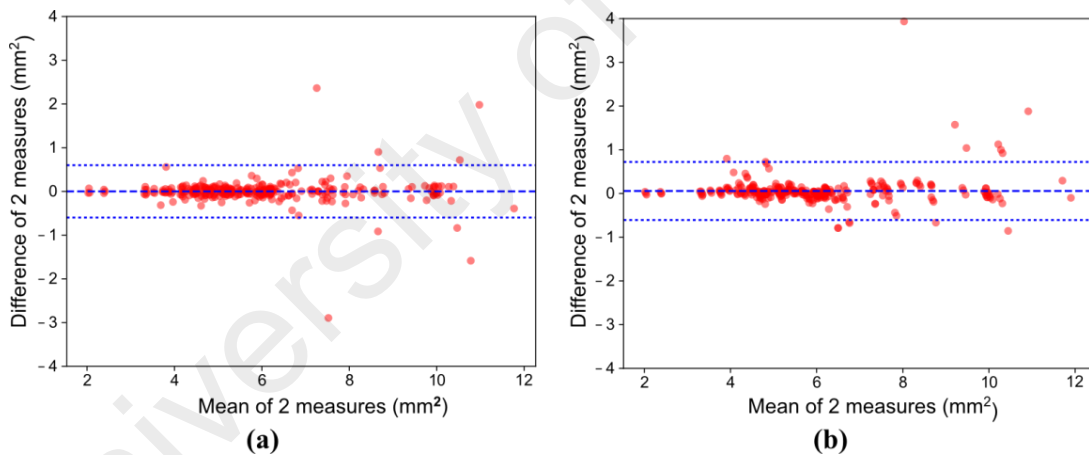


Figure 4.5: Bland-Altman plot analysis of luminal area for all possible pair-comparisons between different observers (a) and between CNN and observers (b) for the 100 randomly selected images from the test set.

CHAPTER 5: DISCUSSION

Lumen dimension is an important factor in the optimization of percutaneous coronary intervention. This measure allows the clinician to localize and measure the length of lesions along the vessel wall before making an optimum selection of stent for deployment. It also allows one to indirectly assess the quality of stenting (i.e. based on total expansion of the narrowed artery) and is the first step towards quantifying the amount of stent malapposition. Misinterpretation of lesion location and length results in both clinical and financial consequences as additional stents are required for redeployment, and overlapping of multiple stents are often associated with increase incidences of restenosis, thrombosis and adverse clinical outcomes (Suzuki, 2014).

Manually quantifying coronary lumen dimension from IVOCT images over the entire extent of the imaged segment is currently not clinically feasible in view of the number of sample images available per pullback (i.e. >100 images). Automatic segmentation is desirable but challenging due to the significant variety of image features and artifacts obtained in routine scanning, restricting the operation of most image processing algorithms to a specific subset of good quality images. Deep learning techniques have been shown to be more robust in a pool of heterogeneous input images, and this has also been demonstrated in our results (Tan et al., 2017). Our study represents the first study employing such a technique, combined with a linear regression approach, to the automatic segmentation of lumen from IVOCT images.

The results showed a notable increase in CNN accuracy up to 25 training pullbacks, and incremental improvements thereafter. The median accuracy in luminal radius at each radial location, against a manual gold standard, was $21.87\mu\text{m}$ at optimal training with 45 training pullbacks, which is comparable to the OCT system's axial resolution ($15\mu\text{m}$). The median luminal area was marginally greater by manual segmentation in

comparison to CNN segmentation (i.e. 5.28 mm² vs 5.26 mm²), yielding a median error of 1.38% (i.e. significantly <2% at $p = 0.001$). The CNN also has good limits of agreement against all observers (± 0.665 mm²), which is comparable with the limit of agreement among all observers (± 0.599 mm²).

Published algorithms have required the prior removal of guide-wires or blood artifacts in the images as well as interpolation of output contours across bifurcation and guidewire shadow (Abdolmanafi et al., 2017; Celi & Berti, 2014; Prentašić et al., 2016; Ughi, Adriaenssens, Desmet, & D'hooge, 2012) in order to complete an accurate segmentation. Our linear-regression CNN algorithm did not require such pre- and post-processing of the data, with the behavior across these features arising implicitly from the training data. In addition, the proposed method works on a wide spectrum of IVOCT images whether in presence or absence of stent struts. This approach was determined to be of utility in assessing patient both pre- and post-stenting. Furthermore, the CNN segmentation was able to segment images regardless of stent types and no prior information on implanted type is needed, as can be required by some other segmentation techniques (Giovanni Jacopo Ughi et al., 2012), making it applicable in a wider range of clinical settings.

While training time was significant (13.8 hours for 45 training pullbacks), this is all pre-computed prior to clinical usage. The subsequent time to process a test image was extremely small (40.6 ms). This is an advantage of the proposed method. Thus, the use of linear-regression CNNs offers the potential of intra-operative assessment of the vessel lumen during an intervention.

Limitations of the algorithm occur at areas with highly irregular lumen shapes, and at major bifurcations, where vessel lumen of the main branch is ambiguous even for manual segmentation. This is the main disadvantage of the current method. The

implementation of the algorithm has adopted a 2D processing approach where each image is processed independently. Extending this to a volumetric approach, where adjacent slices influence the segmentation of each image, may result in more stable results in these situations. Alternatively, some form of energy minimization approach may be incorporated into the CNN cost function to enforce additional regularization of the lumen shape.

University of Malaya

CHAPTER 6: CONCLUSION

This study has demonstrated a novel linear-regression CNN for the segmentation of vessel lumen in IVOCT images. The algorithm was tested on clinical data and compared against a manual gold-standard. Results suggested that the CNN provided accurate estimates of the lumen boundary, with errors comparable to the inter-observer variability between multiple human observers. In addition, the algorithm was fast, processing test images at a rate of 40.6 ms per image. Our results suggest that linear-regression CNN-based approach has the potential to be incorporated into a clinical workflow and provide quantitative assessment of vessel lumen in an intra-operative timeframe.

Therefore, it is concluded that the proposed method was able to facilitate quantitative assessment of coronary artery stenosis and stent placement by extracting coronary lumen from optical coherence tomography images using a fully automated segmentation framework. It was also demonstrated that the proposed method was feasible for clinical adoption, facilitating an accurate and robust coronary artery disease diagnosis in a wide spectrum of clinical OCT images.

6.1 Future works

Future work will include enhancing the CNN segmentation to include segmentation of other features pertaining to coronary artery diseases such as lipid pools, plaque and thrombus. In addition, the incorporation of other modalities in the framework such X-ray angiography or 3D segmentation could generate a more accurate models of the artery for assessment. Studies to improve and develop new coronary artery segmentation methods will no doubt enhance the current assessment methods as well as improving the quality of intervention to treat coronary artery disease.

REFERENCES

- Abdolmanafi, A., Duong, L., Dahdah, N., & Cheriet, F. (2017). Deep feature learning for automatic tissue classification of coronary artery using optical coherence tomography. *Biomedical Optics Express*, 8(2), 1203-1220.
- Adriaenssens, T., Ughi, G. J., Dubois, C., Onsea, K., De Cock, D., Bennett, J., . . . Belmans, A. (2014). Automated detection and quantification of clusters of malapposed and uncovered intracoronary stent struts assessed with optical coherence tomography. *The international journal of cardiovascular imaging*, 30(5), 839-848.
- Amato, F., López, A., Peña-Méndez, E. M., Vañhara, P., Hampl, A., & Havel, J. (2013). Artificial neural networks in medical diagnosis. *Journal of Applied Biomedicine*, 11(2), 47-58.
- American Heart Association. (2017, March, 2017). Cardiac procedures and surgeries. Retrieved September 20, 2017, from http://www.heart.org/HEARTORG/Conditions/HeartAttack/PreventionTreatmentofHeartAttack/Cardiac-Procedures-and-Surgeries_UCM_303939_Article.jsp#.VpXfr_195D
- Auricchio, F., Conti, M., Ferrazzano, C., & Sgueglia, G. A. (2014). A simple framework to generate 3D patient-specific model of coronary artery bifurcation from single-plane angiographic images. *Computers in Biology and Medicine*, 44(0), 97-109.
- Bengio, Y., Goodfellow, I. J., & Courville, A. (2015). Deep learning. *Nature*, 521(7553), 436-444.
- Bezerra, H. G., Costa, M. A., Guagliumi, G., Rollins, A. M., & Simon, D. I. (2009). Intracoronary Optical Coherence Tomography: A Comprehensive Review: Clinical and Research Applications. *JACC: Cardiovascular Interventions*, 2(11), 1035-1046.
- Boykov, Y. Y., & Jolly, M.-P. (2001). *Interactive graph cuts for optimal boundary & region segmentation of objects in ND images*. Paper presented at the Computer Vision, 2001. ICCV 2001. Proceedings. Eighth IEEE International Conference on.
- Budoff, M. J., Achenbach, S., & Duerinckx, A. (2003). Clinical utility of computed tomography and magnetic resonance techniques for noninvasive coronary angiography. *Journal of the American College of Cardiology*, 42(11), 1867-1878.
- Castelli, W. P. (1998). The new pathophysiology of coronary artery disease. *The American Journal of Cardiology*, 82(10, Supplement 2), 60-65.
- Celi, S., & Berti, S. (2014). In-vivo segmentation and quantification of coronary lesions by optical coherence tomography images for a lesion type definition and stenosis grading. *Medical Image Analysis*, 18(7), 1157-1168.

- Clevert, D.-A., Unterthiner, T., & Hochreiter, S. (2015). Fast and accurate deep network learning by exponential linear units (elus). *arXiv preprint arXiv:1511.07289*.
- De Cock, D., Tu, S., Ughi, G., & Adriaenssens, T. (2014). Development of 3D IVOCT Imaging and Co-Registration of IVOCT and Angiography in the Catheterization Laboratory. *Current Cardiovascular Imaging Reports*, 7(10), 1-14.
- De Franco, A. C., & Nissen, S. E. (2001). Coronary intravascular ultrasound: implications for understanding the development and potential regression of atherosclerosis. *The American Journal of Cardiology*, 88(10, Supplement 1), 7-20.
- Dowsley, T., Al-Mallah, M., Ananthasubramaniam, K., Dwivedi, G., McArdle, B., & Chow, B. J. W. (2013). The Role of Noninvasive Imaging in Coronary Artery Disease Detection, Prognosis, and Clinical Decision Making. *Canadian Journal of Cardiology*, 29(3), 285-296.
- Fang, L., Cunefare, D., Wang, C., Guymer, R. H., Li, S., & Farsiu, S. (2017). Automatic segmentation of nine retinal layer boundaries in OCT images of non-exudative AMD patients using deep learning and graph search. *Biomedical Optics Express*, 8(5), 2732-2744.
- Gonzalo, N., Serruys, P. W., Okamura, T., van Beusekom, H. M., Garcia-Garcia, H. M., van Soest, G., . . . Regar, E. (2009). Optical coherence tomography patterns of stent restenosis. *American Heart Journal*, 158(2), 284-293.
- Goodfellow, I. J., Bengio, Y., & Courville, A. (2016). *Deep Learning*: MIT Press.
- Gurmeric, S., Isguder, G., Carlier, S., & Unal, G. (2009). A New 3-D Automated Computational Method to Evaluate In-Stent Neointimal Hyperplasia in In-Vivo Intravascular Optical Coherence Tomography Pullbacks. In G.-Z. Yang, D. Hawkes, D. Rueckert, A. Noble & C. Taylor (Eds.), *Medical Image Computing and Computer-Assisted Intervention – MICCAI 2009* (Vol. 5762, pp. 776-785): Springer Berlin Heidelberg.
- Havaei, M., Davy, A., Warde-Farley, D., Biard, A., Courville, A., Bengio, Y., . . . Larochelle, H. (2017). Brain tumor segmentation with Deep Neural Networks. *Medical Image Analysis*, 35, 18-31.
- Huang, D., Swanson, E. A., Lin, C. P., Schuman, J. S., Stinson, W. G., Chang, W., . . . Puliafito, C. A. (1991). Optical coherence tomography. *Science*, 254(5035), 1178-1181.
- Jang, I.-K., Bouma, B. E., Kang, D.-H., Park, S.-J., Park, S.-W., Seung, K.-B., . . . Tearney, G. J. (2002). Visualization of coronary atherosclerotic plaques in patients using optical coherence tomography: comparison with intravascular ultrasound. *Journal of the American College of Cardiology*, 39(4), 604-609.
- Kai-Pin, T., Wen-Zhe, S., De Silva, R., Edwards, E., & Rueckert, D. (2011, March 30 2011-April 2 2011). *Automatic vessel wall detection in intravascular coronary OCT*. Paper presented at the Biomedical Imaging: From Nano to Macro, 2011 IEEE International Symposium on.

- Kingma, D., & Ba, J. (2014). Adam: A method for stochastic optimization. *arXiv preprint arXiv:1412.6980*.
- Kristensen, S. D., Ravn, H. B., & Falk, E. (1997). Insights Into the Pathophysiology of Unstable Coronary Artery Disease. *The American Journal of Cardiology*, 80(5, Supplement 1), 5E-9E.
- Kume, T., Akasaka, T., Kawamoto, T., Watanabe, N., Toyota, E., Neishi, Y., . . . Yoshida, K. (2006). Assessment of Coronary Arterial Plaque by Optical Coherence Tomography. *The American Journal of Cardiology*, 97(8), 1172-1175.
- LeCun, Y., Bottou, L., Bengio, Y., & Haffner, P. (1998). Gradient-based learning applied to document recognition. *Proceedings of the IEEE*, 86(11), 2278-2324.
- Lee, C. S., Tying, A. J., Deruyter, N. P., Wu, Y., Rokem, A., & Lee, A. Y. (2017). Deep-learning based, automated segmentation of macular edema in optical coherence tomography. *Biomedical Optics Express*, 8(7), 3440-3448.
- Li, Q., Cai, W., Wang, X., Zhou, Y., Feng, D. D., & Chen, M. (2014, 10-12 Dec. 2014). *Medical image classification with convolutional neural network*. Paper presented at the 2014 13th International Conference on Control Automation Robotics & Vision (ICARCV).
- Mauri, L., O'Malley, A. J., Popma, J. J., Moses, J. W., Leon, M. B., Holmes, D. R., . . . Kuntz, R. E. (2005). Comparison of thrombosis and restenosis risk from stent length of sirolimus-eluting stents versus bare metal stents. *The American Journal of Cardiology*, 95(10), 1140-1145.
- Mobley, B. A., Schechter, E., Moore, W. E., McKee, P. A., & Eichner, J. E. (2000). Predictions of coronary artery stenosis by artificial neural network. *Artificial Intelligence in Medicine*, 18(3), 187-203.
- Nekovei, R., & Ying, S. (1995). Back-propagation network and its configuration for blood vessel detection in angiograms. *Neural Networks, IEEE Transactions on*, 6(1), 64-72.
- Nissen, S. (2001). Coronary angiography and intravascular ultrasound. *The American Journal of Cardiology*, 87(4, Supplement 1), 15-20.
- Otsu, N. (1975). A threshold selection method from gray-level histograms. *Automatica*, 11(285-296), 23-27.
- Patwari, P., Weissman, N. J., Boppart, S. A., Jesser, C., Stamper, D., Fujimoto, J. G., & Brezinski, M. E. (2000). Assessment of coronary plaque with optical coherence tomography and high-frequency ultrasound. *The American Journal of Cardiology*, 85(5), 641-644.
- Phipps, J. E., Vela, D., Hoyt, T., Halaney, D. L., Mancuso, J. J., Buja, L. M., . . . Feldman, M. D. (2015). Macrophages and Intravascular OCT Bright Spots: A Quantitative Study. *JACC: Cardiovascular Imaging*, 8(1), 63-72.

- Prati, F., Regar, E., Mintz, G. S., Arbustini, E., Di Mario, C., Jang, I.-K., . . . Grube, E. (2010). Expert review document on methodology, terminology, and clinical applications of optical coherence tomography: physical principles, methodology of image acquisition, and clinical application for assessment of coronary arteries and atherosclerosis. *European heart journal*, 31(4), 401-415.
- Prentašić, P., Heisler, M., Mammo, Z., Lee, S., Merkur, A., Navajas, E., . . . Lončarić, S. (2016). Segmentation of the foveal microvasculature using deep learning networks. *Journal of Biomedical Optics*, 21(7), 075008-075008.
- Rokach, L., & Maimon, O. (2005). Clustering Methods. In O. Maimon & L. Rokach (Eds.), *Data Mining and Knowledge Discovery Handbook* (pp. 321-352). Boston, MA: Springer US.
- Schindelin, J., Rueden, C. T., Hiner, M. C., & Eliceiri, K. W. The ImageJ ecosystem: An open platform for biomedical image analysis. (1098-2795 (Electronic)).
- Slager, C. J., Wentzel, J. J., Schuurbiens, J. C., Oomen, J. A., Kloet, J., Krams, R., . . . De Feyter, P. J. (2000). True 3-dimensional reconstruction of coronary arteries in patients by fusion of angiography and IVUS (ANGUS) and its quantitative validation. *Circulation*, 102(5), 511-516.
- Suzuki, K. (2014). *Mining of Training Samples for Multiple Learning Machines in Computer-Aided Detection of Lesions in CT Images*. Paper presented at the Data Mining Workshop (ICDMW), 2014 IEEE International Conference on.
- Tan, L. K., Liew, Y. M., Lim, E., & McLaughlin, R. A. (2017). Convolutional neural network regression for short-axis left ventricle segmentation in cardiac cine MR sequences. *Medical Image Analysis*, 39, 78-86.
- Tearney, G. J., Regar, E., Akasaka, T., Adriaenssens, T., Barlis, P., Bezerra, H. G., . . . Weisz, G. (2012). Consensus Standards for Acquisition, Measurement, and Reporting of Intravascular Optical Coherence Tomography Studies: A Report From the International Working Group for Intravascular Optical Coherence Tomography Standardization and Validation. *Journal of the American College of Cardiology*, 59(12), 1058-1072.
- Tearney, G. J., Waxman, S., Shishkov, M., Vakoc, B. J., Suter, M. J., Freilich, M. I., . . . Bouma, B. E. (2008). Three-Dimensional Coronary Artery Microscopy by Intracoronary Optical Frequency Domain Imaging. *JACC: Cardiovascular Imaging*, 1(6), 752-761.
- Tearney, G. J., Yabushita, H., Houser, S. L., Aretz, H. T., Jang, I. K., Schlendorf, K. H., . . . Bouma, B. E. (2003). Quantification of macrophage content in atherosclerotic plaques by optical coherence tomography. *Circulation*, 107(1), 113-119.
- Tu, J. V. (1996). Advantages and disadvantages of using artificial neural networks versus logistic regression for predicting medical outcomes. *Journal of Clinical Epidemiology*, 49(11), 1225-1231.

- Ughi, G. J., Adriaenssens, T., Desmet, W., & D'hooge, J. (2012). Fully automatic three-dimensional visualization of intravascular optical coherence tomography images: methods and feasibility in vivo. *Biomedical Optics Express*, 3(12), 3291-3303.
- Ughi, G. J., Adriaenssens, T., Onsea, K., Kayaert, P., Dubois, C., Sinnaeve, P., . . . D'hooge, J. (2012). Automatic segmentation of in-vivo intra-coronary optical coherence tomography images to assess stent strut apposition and coverage. *The international journal of cardiovascular imaging*, 28(2), 229-241.
- Wang, A., Eggermont, J., Dekker, N., Garcia-Garcia, H., Pawar, R., Reiber, J. C., & Dijkstra, J. (2013). Automatic stent strut detection in intravascular optical coherence tomographic pullback runs. *The international journal of cardiovascular imaging*, 29(1), 29-38.
- World Health Organization. (2014). *Global Status Report on Noncommunicable Diseases 2014*.
- Yabushita, H., Bouma, B. E., Houser, S. L., Aretz, H. T., Jang, I. K., Schlendorf, K. H., . . . Tearney, G. J. (2002). Characterization of human atherosclerosis by optical coherence tomography. *Circulation*, 106(13), 1640-1645.

LIST OF PUBLICATIONS AND PAPERS PRESENTED

Journal publication:

Yan Ling Yong, Li Kuo Tan, Robert A. McLaughlin, Kok Han Chee, Yih Miin Liew.
2017. Linear-regression convolutional neural network for fully automated coronary lumen segmentation in intravascular optical coherence tomography. Journal of Biomedical Optics. (Accepted)

Conference:

Yan Ling Yong, Kok Han Chee, Li Kuo Tan, Robert A. McLaughlin, Yih Miin Liew.
Convolutional neural network for coronary lumen segmentation in intravascular optical coherence tomography. , Presented at International Technical Postgraduate Conference (Tech Post 2017), Kuala Lumpur, 2017-04-05 to 2017-04-06.